Supporting Information

Spider Dragline Silk-Inspired 3D Printed Sustainable Zinc ion Battery with Ultrahigh Stability

Hongyu Lu, Jisong Hu, Botao Jiang, Kaiqi Zhang, Zhengyu Ju, Gehong Su, Yuanyuan Gao, Zhaodan Fu, Jingxin Zhao,* Bingang Xu,* and Guihua Yu**

Dr.H. Lu, Y Gao, Prof. B. Xu

Nanotechnology Center, Research Institute for Intelligent Wearable Systems, The Hong Kong Polytechnic University, Hung Hom, Kowloon, Hong Kong 999077, P. R. China

E-mail: tcxubg@polyu.edu.hk

J. Hu

Advanced Materials and Devices Laboratory, School of Materials Science and Engineering, School of Chemistry and Environmental Engineering, Hanshan Normal University, Chaozhou, 521041, P. R. China

B. Jiang

Department of Materials Science and Engineering, City University of Hong Kong, Hong Kong 999077, P. R. China

Dr. Z. Ju, Prof. G. Yu

Materials Science and Engineering Program and Walker Department of Mechanical Engineering, The University of Texas at Austin, Austin, TX, 78712, USA

E-mail: ghyu@austin.utexas.edu

Z. Fu, G. Su

Sichuan Agricultural University, Ya'an, 625014, P. R. China

E-mail: gehongsu@sicau.edu.cn

Prof. J. Zhao

E-mail: zjingxin@eduhk.hk

Key Laboratory of Low Dimensional Materials and Application Technology of Ministry of Education, School of Materials Science and Engineering, Xiangtan University, Xiangtan, 411105, P. R. China

Table of Content

Fig. S17 The electrochemical performance of D-MXene/ZP anode. Long-term cycling voltage profiles of symmetric cells at current density of **a** 2 mA cm^{-2} and **b** 10 mA cm^{-2}. **c** Coulombic efficiencies test. **d** Tafel curves. **e** EIS curves.

Fig. S18 CV curves of rSP/MXene/ZP and bare ZP anodes.

Fig. S19 Tafel curves of rSP/MXene/ZP, MXene/ZP and bare ZP anodes.

Fig. S20 Exchange current density curves at various rates in rSP/MXene/ZP, MXene/ZP and bare ZP symmetric cells.

Fig. S21 Voltage profiles of the **a** rSP/MXene/ZP anode and **b** MXene/ZP anode c bare ZP anode at 5 mA cm^{-2}.

Fig. S22 Long-term galvanostatic cycling of symmetrical rSP/MXene/ZP symmetric cells at high DOD: **a** 88.5%, **b** 65% and **c** 50%.

Fig. S23 High-resolution XPS spectrums of rSP/MXene/ZP anode before cycling **a** Ti2p. rSP/MXene/ZP anode after cycling **b** Ti2p. **c** EIS curves of the rSP/MXene/ZP and MXene/ZP anodes after cycling. **d** Cross-sectional SEM image of the rSP/MXene/ZP anode after cycling.

Fig. S24 Ex-situ SEM images of MXene/ZP.

Fig. S25 rSP/MXene/ZP anode at different cycles time corresponding materials volume ratios.

Fig. S26 Chronoamperometry curves of rSP/MXene/ZP and bare ZP anodes.

Fig. S27 In-situ monitoring of H_2 evolution flux of **a** rSP/MXene/ZP, **b** bare ZP and **c** MXene/ZP anodes.

Fig. S28 Calculated H adsorption free energies (ΔG_{H^*}) of bare ZP, Zn/rSA, and Zn/Am.

Fig. S29 Adsorption configurations and adsorption energies of H_2O, Am, rSA, and the rSP fragment on Zn(002).

Fig. S30 Nyquist plots at different temperatures for **a** bare ZP, **b** MXene/ZP and **c** rSP/MXene/ZP symmetric cells **d** Corresponding Arrhenius curves and comparison of activation energies.

Fig. S31 a SEM images of PAQS and **b** G-PAQS. **c** XRD spectrum of PAQS and G-PAQS. **d** Raman spectrum of G-PAQS, PAQS and rGO.

Fig. S32 GCD curves of rSP/MXene/ZP//G-PAQS and bare ZP//G-PAQS full cells.

Fig. S33 CV curves of **a** rSP/MXene/ZP//G-PAQS and **b** bare ZP//G-PAQS full cells at different scan rates.

Fig. S34 Log(i) versus log(v) plots at each redox peak.

Fig. S35 Normalized capacity contributions of **a** rSP/MXene/ZP//G-PAQS full cell and **b** bare ZP//G-PAQS full cell at different scan rates from 0.5 to 10 mV s^{-1}.

Fig. S36 GITT curves of **a** rSP/MXene/ZP//G-PAQS full cell, **b** bare ZP//G-PAQS full cell at 1 A g^{-1}.

Fig. S37 GCD curves of single cell and five cells connected in series.

Fig. S38 Voltage profiles of symmetric cells with r-rSP/MXene/ZP anode in a $ZnSO_4$ and b $Zn(OTf)_2$.

3. Supporting Movies

Movie S1. rSP/MXene/ZP//G-PAQS cell pack driving a tesla coil to illuminate a neon lamp.

Movie S2. Conceptual demonstration of energy conversion through magnetic induction coil for r-rSP/MXene/ZP//G-PAQS soft-pack cell pack.

4. Supporting Tables

Table S1. Comparison of the DOD and Cumulative capacity of rSP/MXene/ZP Symmetric cell with recently reported Zn||Zn cells.

Table S2. Lifespan comparison between this work and recently published studies.

Table S3. Comparison of the assembled rSP/MXene/ZP//G-PAQS full cell with the previously reported aqueous Zn ion battery.

1. Experimental Procedures

1.1 Recovery of waste algae and extraction of alginate.

Weigh 50 g of recycled scrap seaweed and add water at a weight ratio of 10:1 (water to seaweed). Soak the kelp at room temperature for 4 h, and add an appropriate amount of formaldehyde to achieve an initial concentration of 1.0%. This process fixes the kelp pigments within the epidermal cells, preventing the pigments from dissolving in water, which would otherwise darken the product's color. Additionally, formaldehyde has a destructive effect on the plant cell wall fibers, facilitating the displacement and dissolution of alginates during the digestion process. After soaking, remove the kelp and wash it with water until the wash water is colorless. The chopped seaweed was digested for 24 h at 50℃ by adding 25g Na_2CO_3. After digestion, the seaweeds turn into a paste. It is initially filtered once using gauze, and then the filtrate is vacuum-filtered using a vacuum pump. The filtered solution was diluted with water, and then dilute hydrochloric acid was slowly added to the solution until flocculent precipitates began to form. The mixture was then allowed to stand for 8-12 h. Subsequently, dilute hydrochloric acid was slowly added to the standing solution to adjust the pH to 1-2, causing the alginic acid to coagulate into acid gelatinous lumps. At room temperature, a sodium carbonate solution of a certain concentration was added while stirring until the pH reached 7.5, completing the neutralization process. A certain amount of ethanol was then added to the neutralized solution to precipitate sodium alginate. The precipitated sodium alginate was filtered to remove excess liquid. The filtered sodium alginate was vacuum-dried at 75°C for 12 h to remove moisture. Finally, the dried sodium alginate was ground to obtain the final product.

1.2 Synthesis of poly (2,6-anthraquinone) sulfide (PAQS).

100 mL of anhydrous N-methylpyrrolidone (NMP) solution was poured into a three-necked flask. Subsequently, a mixture of 2,6-dibromoanthraquinone (2.2 g, 6 mmol) and Na_2S (0.47 g, 6 mmol) was added under an argon atmosphere. The mixture was stirred and heated in an oil bath at 200 °C under argon for 24 h. After cooling to room temperature, the mixture was centrifuged and washed several times with NMP, water, and acetone. The solid was then vacuum-dried at 70 °C for more than 24 h, yielding a reddish-brown powder.

1.3 Synthesis and decortication of $Ti_3C_2T_x$.

Firstly, 1.96 g of lithium fluoride (LiF) was dissolved into 22 mL of 9M HCl aqueous solution under an argon atmosphere. Then, 2 g of Ti_3AlC_2 powder was added to the above solution within 15 minutes to avoid overheating of the solution due to the exothermic feature of the reaction. The mixture was continuously stirred for 48 hours at 35 °C, and the residual solid was washed with deionized water and centrifuged (3500 rpm) until the pH of the supernatant reached about 6~7. The final product containing a

small amount of water was filtered by a polyvinylidene fluoride filter and vacuum dried at 60 °C overnight to obtain multilayer $Ti_3C_2T_x$ powder. Afterwards, as-prepared $Ti_3C_2T_x$ powder was dispersed in degassed water, and the weight ratio of $Ti_3C_2T_x$ and water was 1:25. The suspension was ultrasonically vibrated for 40 minutes, then centrifuged at 3500 rpm for 1 hour, and the supernatant was collected, which consisted of a colloidal solution of layered $Ti_3C_2T_x$ flakes with a concentration of about 2.3 mg mL^{-1}.

1.4 Preparation of printable inks.

The previously collected colloidal solution of a few layers of $Ti_3C_2T_x$ flakes was freeze-dried to obtain a few layers of $Ti_3C_2T_x$ powder. To obtain MXene/ZnP inks, 0.11 g of PVP-K30 was dissolved in 6 mL of deionized water and 0.2 g of few layers of $Ti_3C_2T_x$ was slowly added into above solution. After vigorous stirring for 15 h, the mixture was centrifuged at 10000 rpm to remove the supernatant, and finally the concentration of MXene ink (120 mg mL^{-1}) was realized. Subsequently, 0.2 g of zinc powder was dispersed in the concentrated ink of MXene and the zinc powder was well dispersed in the mixed suspension by intense stirring for 4 h and ultrasonic treatment for 1 h, thereby completing the preparation of the MXene/ZP ink.

For the preparation of the rSP/MXene/ZP composite ink, 0.5 g of acrylamide and 1.7 mg of N,N'-methylenebisacrylamide were sequentially added into 4 mL of degassed deionized water and stirred until completely dissolved. Subsequently, after the solution was heated to 60 ℃, 0.36 g of rSA powder was added and stirred until completely dissolved to obtain viscous liquid. And then 0.2 g of zinc powder was slowly added to the viscous liquid and stirred evenly. After cooling the mixture, MXene with different mass fractions (5%, 10%, 15%, 20%, and 25%) were added to the above solution, followed by continuous low-temperature ultrasonic treatment for 2 h and stirring for 12 h to prepare mixed inks with different MXene contents. The G-PAQS ink was prepared by mixing 0.31 g of rGO, 0.2 g PAQS powder and 10 mL deionized water and then concentrating it to 150 mg mL^{-1}.

1.5 3D printing electrode.

As-prepared inks were used to build 3D periodic anode and cathode via modified Regenovo (Bio-Architect® X) 3D printing systematization equipment. The previously prepared printable ink was filled into a syringe with a nozzle (the inner diameter of the nozzle was 220 μm). The moving speed of the nozzle is 10 mm s^{-1}, and the whole process is controlled by G code. It is worth noting that during the rSP/MXene/ZP printing process, multi-band UV light source (with UVA and UVB bands used for deep and surface cross-linking, respectively) is employed to initiate the internal dual-network cross-linking. After printing, all of aerogel electrode were transfer to frozen dryer and freeze dried for at least 24 h to ensure the microstructure stability of aerogel electrode.

1.6 Regeneration of rSP/MXene/ZP anode.

The used battery was disassembled, and the spent rSP/MXene/ZP zinc anode was placed in a 1 M H_2SO_4 solution. During this process, the H_2SO_4 reacted with the zinc deposits to produce hydrogen gas bubbles and $ZnSO_4$. Subsequently, the electrode was ground and stirred for 12 h to ensure a thorough reaction with the sulfuric acid. The reacted solution was then subjected to high-speed centrifugation to separate the supernatant from the precipitate. The supernatant was concentrated to obtain recycled 2M zinc sulfate as the electrolyte. The precipitate was washed several times with deionized water and filtered to obtain the recycled rSP/MXene dual-network carrier, which was then dried overnight at 60°C under vacuum to yield a dry powder. For the preparation of the r-rSP/MXene/ZP ink, 0.27 g of the recycled rSP/MXene powder was added to 8 mL of degassed deionized water and stirred for 12 h to form a uniformly dispersed ink. Additionally, the ink was concentrated by centrifugation to remove excess water, and 0.2 g of zinc powder was added, followed by mechanical stirring and ultrasonic dispersion for several hours to complete the ink preparation. The electrode printing process remained consistent with the previous method.

1.7 Characterizations and electrochemical measurements.

X-ray diffraction (XRD) tests were performed to investigate the crystallinity of samples on Bruker X-ray diffraction system (D8 Advance) with Cu Kradiation. The morphology and microstructure were characterized using a field-emission scanning electron microscope (SEM, Zeiss Merlin Compact) equipped with energy-dispersive spectroscopy (EDS) for elemental analysis. High-resolution transmission electron microscopy (HRTEM) observations were carried out on a JEM-2100F. Nitrogen adsorption/desorption isotherms and pore size distribution were collected on an ASAP 2020 surface area analyzer. FT-IR spectra were carried on (Nicolet is50) FT-IR spectrophotometer. The Raman spectra were recorded via a inVia-Reflex HR confocal Raman instrument with an excitation wavelength of 532 nm. The X-ray photoelectron spectroscopy (XPS) of electrode materials were implemented by an ESCALAB 250Xi X-ray photoelectron spectrometer. The internal morphology of the electrode was non-destructively imaged using X-ray 3D-CT (Xradia 520 Versa).

All electrochemical performance tests were carried out at room temperature. The as-prepared samples were employed as Zn anodes, with 3 M $Zn(OTf)_2$ serving as the electrolyte and glass fiber (Whatman) as the separator. Electrochemical characterization of symmetrical cells with bare ZP, MXene/ZP and rSP/MXene/ZP anodes conducted using 2032-type coin (canrd) cells. In addition, symmetric Zn/Zn cells and asymmetric Zn/Cu cells were used for plating-stripping tests. The galvanostatic charge-discharge curves and the stripping curves were obtained using the Neware battery

testing system (CT-4000Q, Shenzhen, China). Linear sweep voltammetry (LSV), cyclic voltammetry (CV), Chronoamperometry (CA) and Tafel curves were carried on an electrochemical (CHI660E, Shanghai, China). The zinc-organic full battery employs rSP/MXene/ZP as the anode and PAQS as the cathode, with 3M $Zn(OTf)_2$ aqueous solution serving as the electrolyte. The battery was assembled in a CR2032-type stainless steel coin cell case, with a glass fiber separator isolating the cathode and anode. To ensure sufficient electrolyte supply, the rSP/MXene/ZP anode was fully soaked in 3M $Zn(OTf)_2$ electrolyte beforehand, allowing its three-dimensional porous network structure to absorb and store an adequate amount of electrolyte. Upon cell assembly, an additional 145 μL of excess electrolyte was injected to guarantee an abundant electrolyte reserve inside the battery. The galvanostatic charged/discharged test of Zn-organic full cell was carried out in a voltage range of 0.2-1.8 V at different current densities. The electrochemical impedance spectroscopy (EIS) was collected by electrochemical workstation at frequency range of 0.01 Hz to 10^5 Hz. The diffusion coefficient of Zn^{2+} in the full cell was determined by galvanostatic intermittent titration technique (GITT) at current density of 1 A g^{-1}. The bulk ionic conductivity of different zinc anodes measured using the blocking electrode method. The Ti foil was fixed in a plastic splint cell with wetted glass fiber (wetted by 3 M $Zn(OTf)_2$). The ionic conductivity of the hydrogel carrier was also measured by EIS, and the frequency range was 100-10^5 Hz.

1.8 Computational methods.

The calculations in this work were performed using a combination of computational tools tailored to address specific aspects of the problem. The Vienna Ab initio Simulation Package (VASP)[1] was employed to calculate adsorption energies and charge density differences, leveraging its robust implementation of density functional theory (DFT) with a plane-wave basis set and pseudopotentials. For molecular properties such as the lowest unoccupied molecular orbital (LUMO), highest occupied molecular orbital (HOMO), and electrostatic potential (ESP), Gaussian[2] was utilized. Additionally, molecular dynamics (MD) simulations were conducted using the Forcite module in Materials Studio to investigate the dynamic behavior of the systems.

In VASP, the generalized gradient approximation (GGA) with the Perdew-Burke-Ernzerhof (PBE) functional[3] was used to describe the exchange-correlation interactions. The electron–ion interactions were described using the projector augmented-wave (PAW) method.[4] The convergence criteria of energy and force in the calculations were set as 1.0×10^{-5} eV and 0.05 eV/Å, respectively. The Brillouin zone was sampled with a k-point density of 0.04 $Å^{-1}$. To account for van der Waals (vdW) interactions, the DFT-D3 method with Becke-Johnson damping[5] was employed.

To investigate the adsorption capabilities of the Zn surface, a $3\sqrt{3}\times4$ supercell of the Zn(002) surface was selected as the substrate. A plane-wave cutoff energy of 500 eV was used. The Zn(002) slab contained

3 atomic layers, with the bottom 1 layers fixed during relaxation. A vacuum layer thicker than 15 Å was introduced to avoid interactions between periodic images. For the adsorption energy calculations, Am and rSA were first considered as monomeric fragments to identify the local Zn-binding sites. To further account for the cross-linked polymeric structure, an rSP fragment containing both rSA and Am units was also constructed and adsorbed on the Zn(002) surface. The SA molecule was passivated with hydrogen atoms to maintain electrical neutrality. The adsorption energy (E_{ads}) was calculated using the formula:

$$E_{ads} = E_{total} - (E_{surface} + E_{adsorbate})$$

where E_{total} is the total energy of the system with the adsorbed molecule, $E_{surface}$ is the energy of the clean surface, and $E_{adsorbate}$ is the energy of the isolated molecule. A more negative $E_{adsorbate}$ value indicates stronger adsorption.

For the molecular properties, Gaussian[47] was utilized to compute the LUMO, HOMO, and ESP. These calculations were performed at the B3LYP/6-31G level of theory.[6]

Molecular dynamics (MD) simulations were conducted using the Forcite module in Materials Studio. Two systems were considered: (1) a single-network system containing 600 H_2O molecules, 40 Zn^{2+} ions, 65 OTF^- ions, and 5 SA trimer molecules (each carrying a -3 charge); and (2) a dual-network system containing 600 H_2O molecules, 40 Zn^{2+} ions, 65 OTF^- ions, 5 Am trimer molecules, and 15 SA monomer molecules (each carrying a -1 charge). The simulations were performed at 300 K and 1 atm. Initially, the systems were annealed, followed by optimization under the NPT ensemble, and finally equilibrated under the NVT ensemble. The Zn^{2+} diffusion behavior was evaluated from the mean square displacement (MSD), and the diffusion coefficients were used to compare the relative ion-transport capability of different systems.

1.9 Calculation Details.

The specific capacity of rSP/MXene/ZP//G-PAQS full cells are acquired from the discharge curve of GCD tests based on the following equations:

$$C = \frac{\int_0^{\Delta t} idt}{m}$$

Where C (mAh g) is the specific discharge capacity of full cell, i (mA) is discharge current, Δt (h) is the discharge time, and m (mg) represents the mass of the active material on the electrodes.

Furthermore, the energy density of the rSP/MXene/ZP//G-PAQS full cell was calculated based on the following equation:

$$E = \frac{C \times m_{PAQS} \times V}{m_{PAQS}}$$

Where C represents the calculated specific discharge capacity, V indicetes the operating voltage, m_{PAQS}

is the mass of the active material on G-PAQS cathode.

The power density of the rSP/MXene/ZP full cell was calculated by the following equation:

$$P = \frac{E}{t}$$

Where E is the calculated energy density and t is the discharge time of full cell.

The contribution of capacitance behavior of full cell can be qualitatively calculated by the following equations:

$$i = av^b$$

Which can be expressed as:

$$\log(i) = b\log(v) + \log(a)$$

Where i represents the peak current (A), v denotes the corresponding scan rate (V s^{-1}), while a and b are adjustable parameters. The value of b can be obtained from the the linear relation between log (i) and log (v) of the redox peaks. When b = 0.5, the capacitive behavior is diffusion-controlled. The value of b approaches 1.0, the capacitive behavior is determined by the capacitive storage process..

The contributions of capacitive processes and diffusion processes to the overall capacity can be calculated using the following formula:

$$i = k_1 v + k_2 v^{1/2}$$

Which can be reformulated as:

$$i/v^{1/2} = k_1 v^{1/2} + k_2$$

Where i is the current response, k_1v is the capacitance contribution, and $k_2v^{1/2}$ indicates diffusion-controlled contribution. The value of k_1 can be calculated.

The ionic conductivity of all samples could be calculated from the bulk electrolyte resistance by the following equation:

$$\sigma = \frac{L}{R_b S}$$

Where σ is ionic conductivity, L is the thickness of the sample of 0.32 cm, S is the contact area of 0.81 cm^2, R_b is resistance of sample (Bare ZP of 6.01 Ω, MXene/rSP of 7.25 Ω, rSP of 11.14 Ω and rSA of 33.76 Ω).

The depth of discharge (DOD) of rSP/MXene/ZP anode was calculated by the following equation:

$$DOD_{(\%)} = \frac{I \times t \times S}{m \times C_{theoretical}} \times 100\%$$

Where I (mA cm^{-2}) indicates the applied current density, t (h) is the discharge time, m(g) represents mass of zinc powder, S(cm^2) is actual area of electrode, $C_{theoretical}$ is theoretical specific capacity of Zn anode (~819.5 mAh g^{-1}). The active zinc powder mass is 0.0327 g, the rSP/MXene/ZP anode total mass is 0.0956

g. The average zinc powder mass was determined to be 0.0327 g through an acid dissolution method. Specifically, the composite electrodes were immersed in dilute hydrochloric acid to completely dissolve the zinc component, followed by filtration to separate the insoluble residues (MXene, polymers, etc.). The resulting solutions were then weighed using an analytical balance, and the average value was calculated from multiple measurements.

Specifically,

$$DOD_{(50\%)} = \frac{13.4\ mA\,cm^{-2} \times 1\ h \times 1\ cm^{-2}}{0.0327\ g \times 819.5\ mAh\,g^{-1}} \times 100\%$$

$$DOD_{(65\%)} = \frac{17.42\ mA\,cm^{-2} \times 1\ h \times 1\ cm^{-2}}{0.0327\ g \times 819.5\ mAh\,g^{-1}} \times 100\%$$

$$DOD_{(88.5\%)} = \frac{23.72\ mA\,cm^{-2} \times 1\ h \times 1\ cm^{-2}}{0.0327\ g \times 819.5\ mAh\,g^{-1}} \times 100\%$$

2. Supporting Figures and Notes

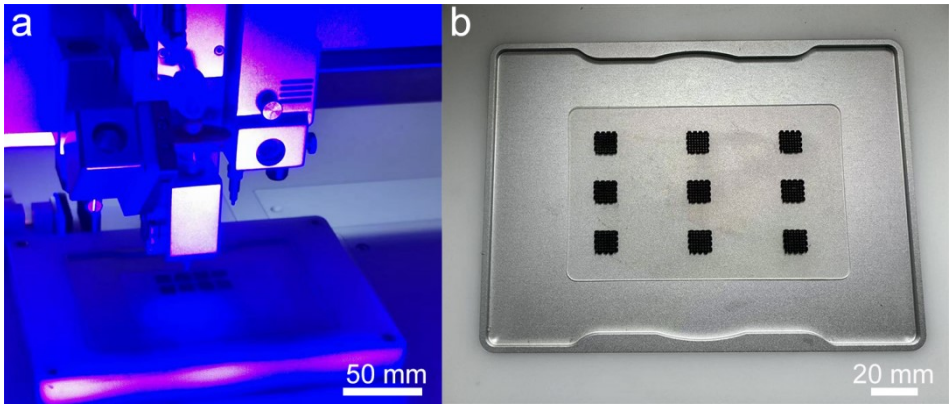

Fig. S1. a The 3D printing process under multi-band UV irradiation and **b** 3D printed dual-network ZPAs.

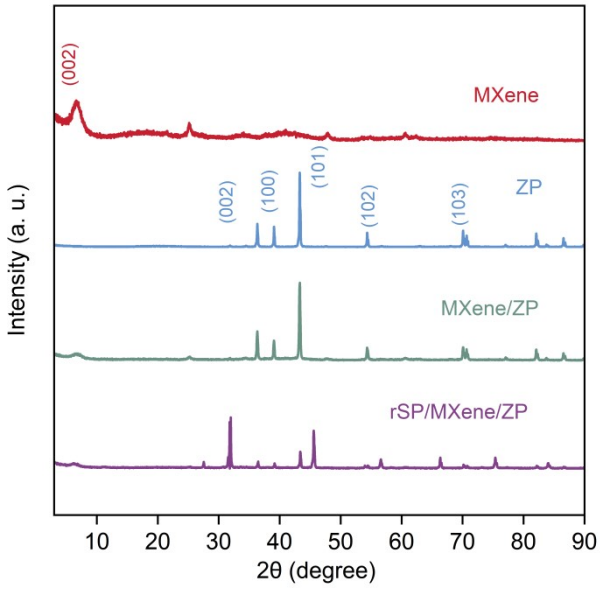

Fig. S2. XRD spectrum of MXene, ZP, MXene/ZP and rSP/MXene/ZP.

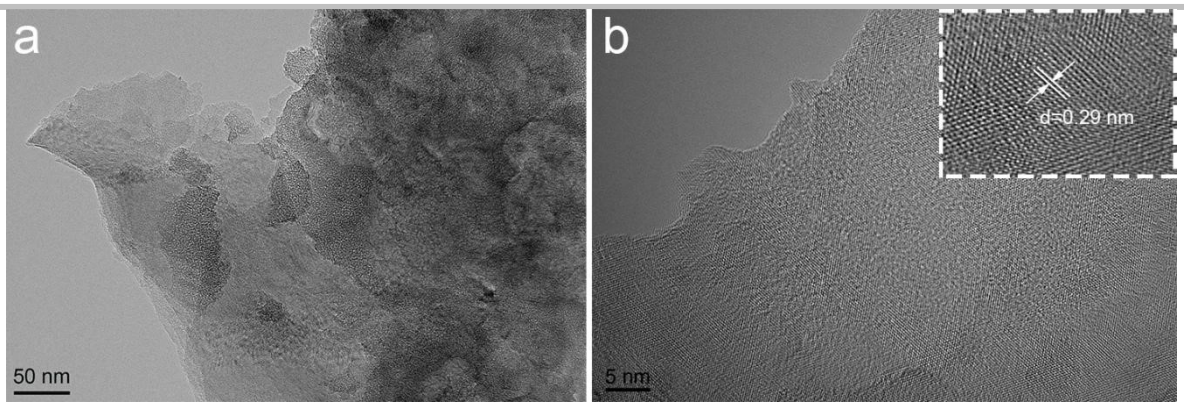

Fig. S3. a TEM and **b** HRTEM images of MXene.

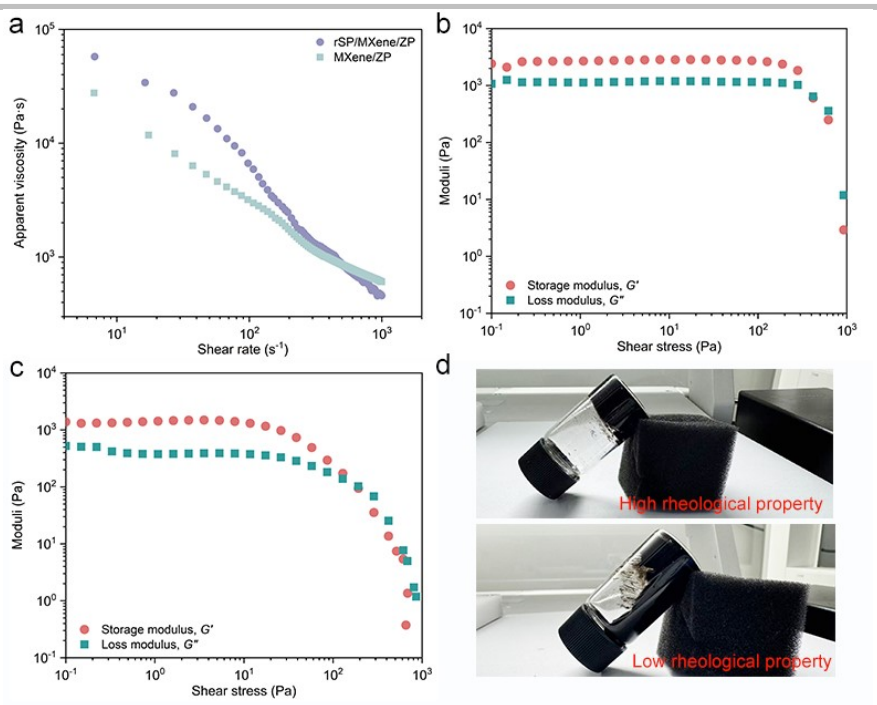

Fig. S4. a The relationship between the apparent viscosity and shear rate for rSP/MXene/ZP and MXene/ZP inks. **b** The relationship between the storage modulus (G′) and loss modulus (G″) and the shear stress for rSP/MXene/ZP and **c** MXene/ZP inks. **d** Optical photographs of inks with different rheological properties.

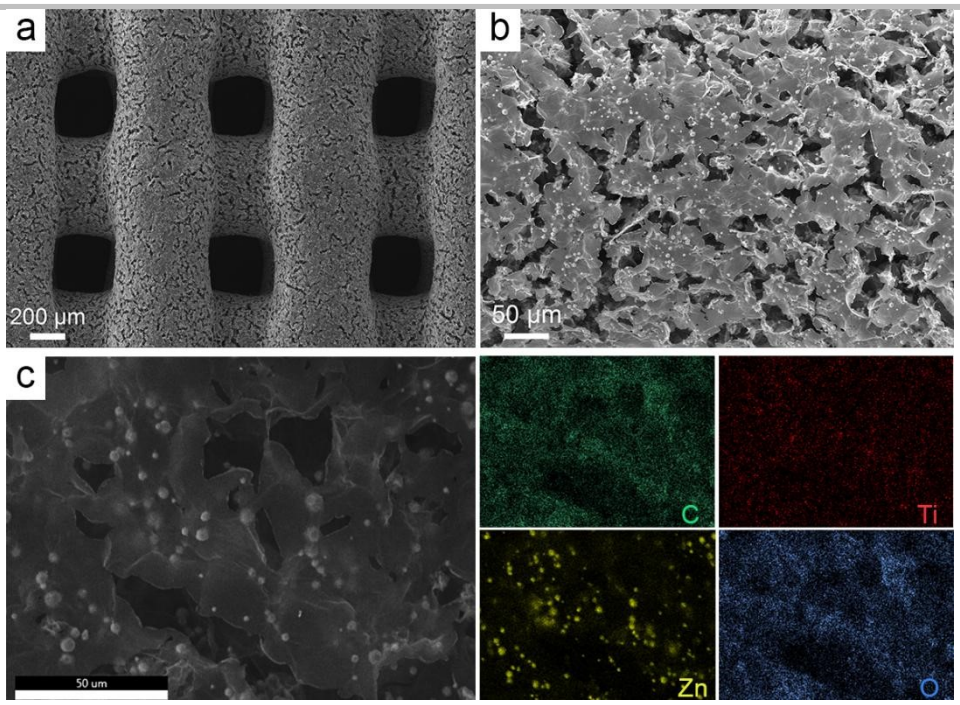

Fig. S5. a-c SEM images of MXene/ZP anode and corresponding EDS mapping.

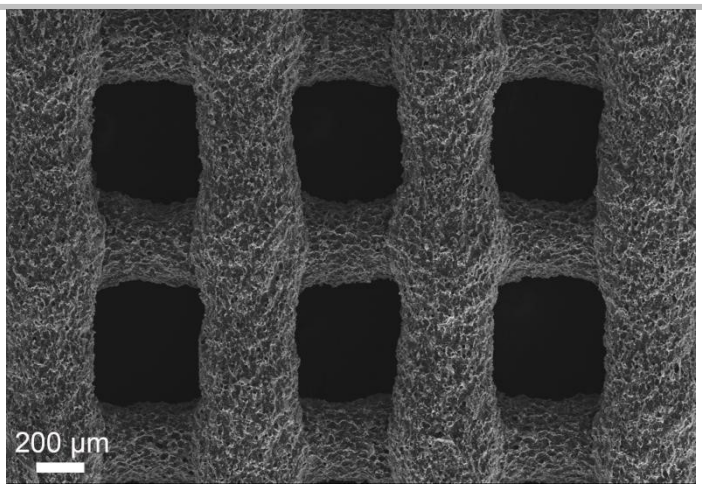

Fig. S6. SEM image of rSP/MXene/ZP anode.

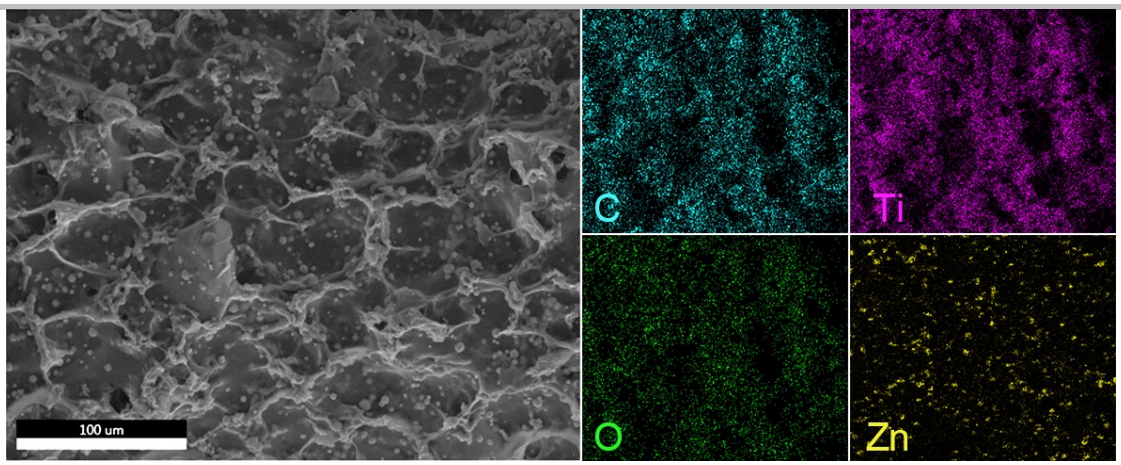

Fig. S7. EDS mapping of the rSP/MXene/ZP anode.

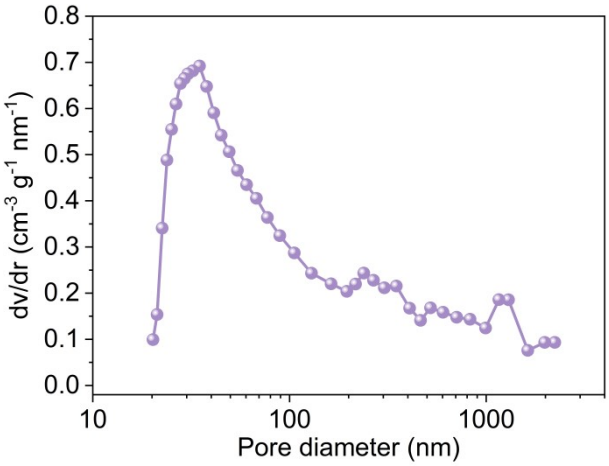

Fig. S8. Barrett-Joyner-Halenda (BJH) pore size distribution of rSP/MXene/ZP.

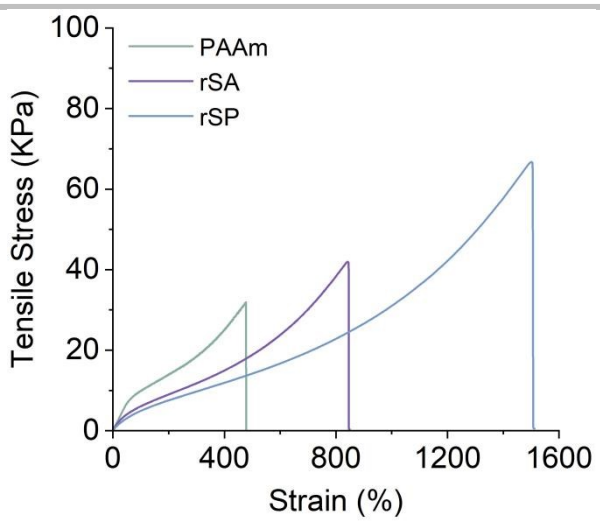

Fig. S9. Mechanical properties of PAAm, rSA and rSP.

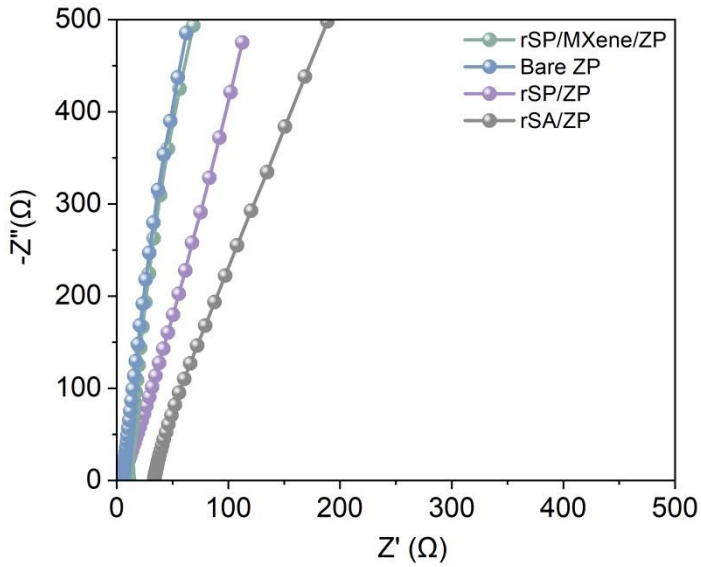

Fig. S10. Nyquist curves of rSP/MXene/ZP, rSP/ZP, rSA/ZP and bare ZP anodes.

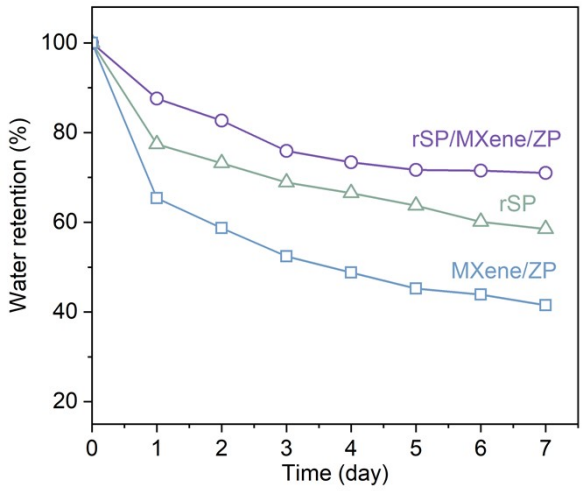

Fig. S11. Water retention rate of rSP/MXene/ZP, rSP and MXene/ZP in 7 days.

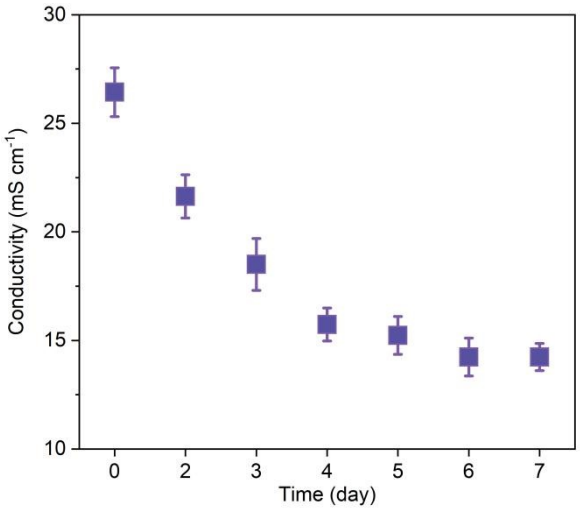

Fig. S12. Changes of ionic conductivity of rSP/MXene/ZP in 7 days.

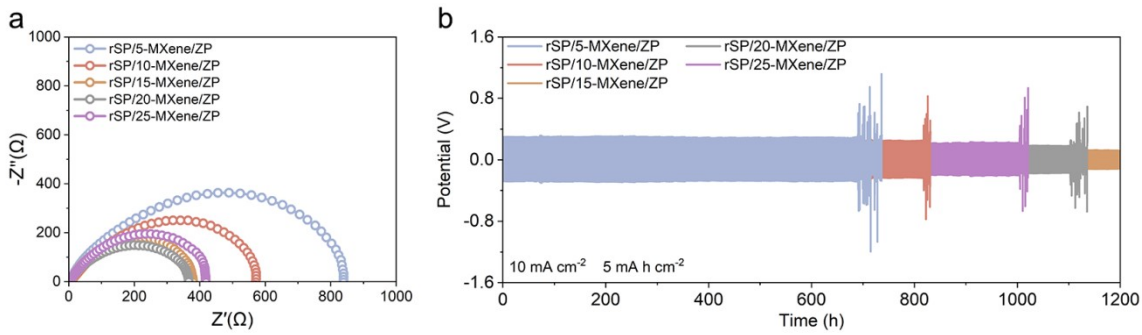

Fig. S13. a EIS curves and **b** voltage profiles of symmetric cells employing rSP/MXene/ZP anodes with various MXene contents.

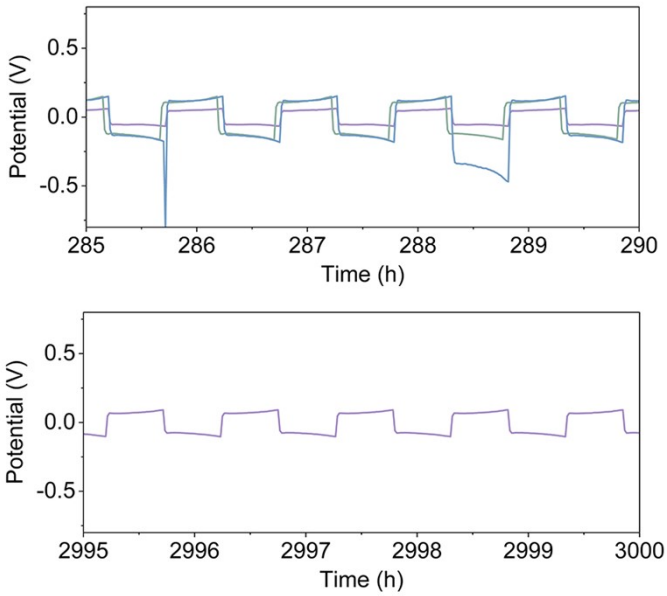

Fig. S14. Voltage profiles of different anodes at the current density of 2 mA cm^{-2}.

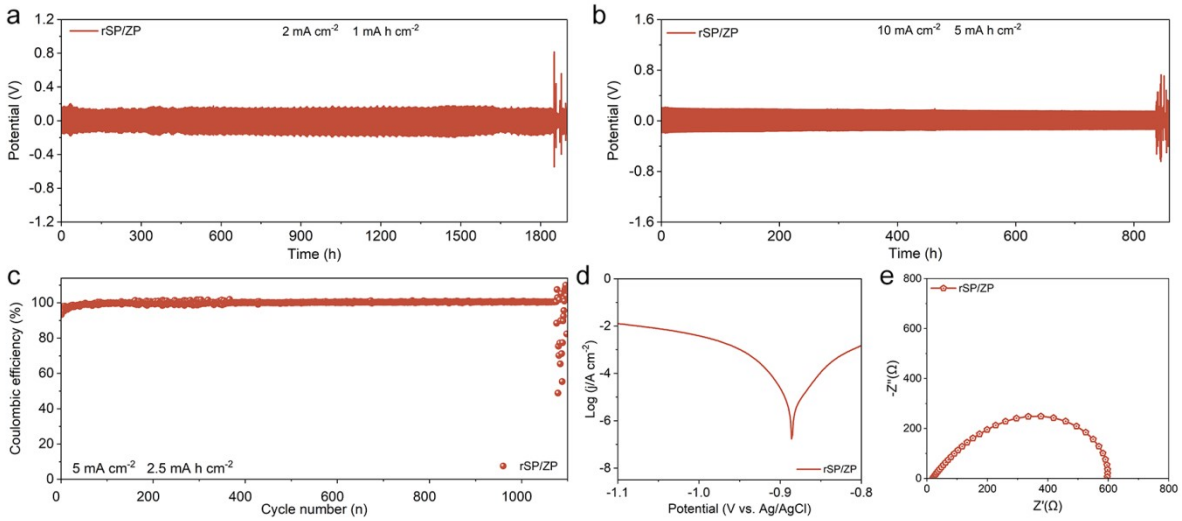

Fig. S15. The electrochemical performance of rSP/ZP anode. Long-term cycling voltage profiles of symmetric cells at current density of **a** 2 mA cm^{-2} and **b** 10 mA cm^{-2}.**c** Coulombic efficiencies test. **d** Tafel curves. **e** EIS curves.

As demonstrated in Figure S15a and Figure 3a, the rSP/ZP anode symmetric cell with an ion-conductive rSP network achieves a cycle life of 1852 h under a current density of 2 mA cm^{-2}, whereas the MXene/ZP anode with an electron-conductive MXene network sustains 1294 h. In contrast, the rSP/MXene/ZP anode featuring a dual ion-electron conductive network exhibits a remarkable advantage, extending the stable cycling lifespan to 3000 h. Notably, even at a high current density of 10 mA cm^{-2}, the rSP/ZP anode and the MXene/ZP anode can maintain stable cycling for 836 h and 636 h, respectively, while the rSP/MXene/ZP dual-network anode achieves a prolonged stable cycling of 1250 h (Figure S15b and Figure 3b). The Coulombic efficiency (CE) of zinc plating/stripping measured by Zn||Cu asymmetric cells is a critical metric for evaluating zinc reversibility. The cell employing rSP/ZP with a single ion-conductive network exhibits a favorable cycling lifespan exceeding 1075 cycles, with an average CE of 99.4%, demonstrating that the rSP network possesses a certain capability for suppressing zinc dendrites. The MXene/ZP cell with a single electron-conductive network achieves stable cycling for 832 cycles. Notably, the rSP/MXene/ZP dual-network system, which combines both networks, exhibits a remarkable advantage, extending the cycling lifespan to 1500 cycles with an enhanced average CE of 99.84% (Figure S15c and Figure 3f). This fully confirms the synergistic effect of the ion-electron dual network in enhancing the interfacial stability of the Zn anode. Tafel polarization measurements further reveal the anti-corrosion properties of the dual-network anode (Figure S15d and Figure S19). Specifically, the MXene/ZP anode exhibits a corrosion potential of -0.892 V, and the rSP/ZP anode shows -0.886 V. In contrast, the rSP/MXene/ZP dual-network anode, which combines the advantages of both networks, demonstrates a significantly more positive corrosion potential of -0.879 V. This result confirms that the synergistic effect of the ion-electron dual network endows it with superior anti-corrosion performance compared to either the single ion-conductive network or the single electron-conductive network alone. In addition, EIS curves reveal that the rSP/MXene/ZP dual-network anode exhibits an impedance of 371.8 Ω, which is significantly lower than that of the rSP/ZP single ion-conductive network (596.4 Ω) and the MXene/ZP single electron-conductive network (425.2 Ω). This result indicates that the incorporation of the MXene electron-conductive network effectively reduces the charge transfer resistance, while the synergistic effect of the rSP ion-conductive network further optimizes interfacial ion transport, enabling the dual-network system to achieve the most favorable interfacial charge transfer kinetics (Figure S15e and Figure 3h). The superior performance of the dual-network originates from the spatially separated yet functionally complementary pathways: the rSP network homogenizes Zn^{2+} flux to prevent dendrite formation, while the MXene network redistributes local electrons to mitigate localized corrosion and dead Zn accumulation.

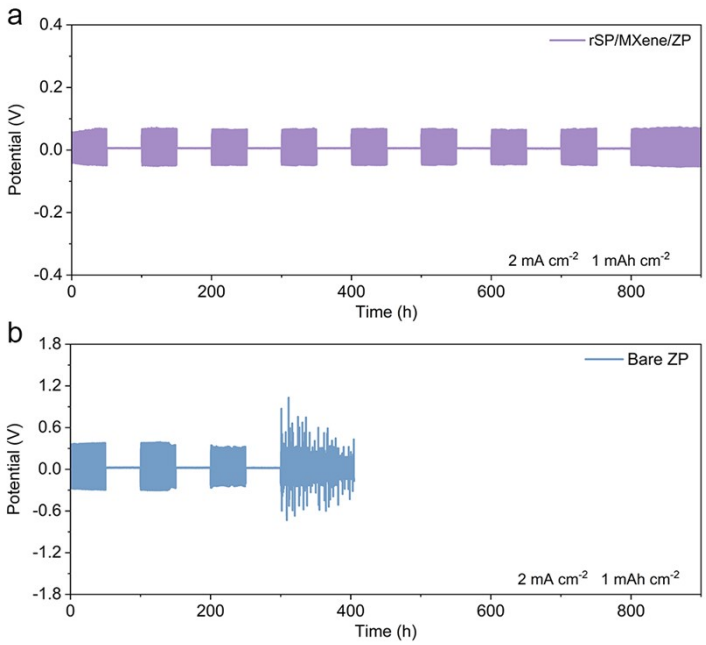

Fig. S16. Shelving recovery property of **a** rSP/MXene/ZP and **b** bare ZP symmetric cells.

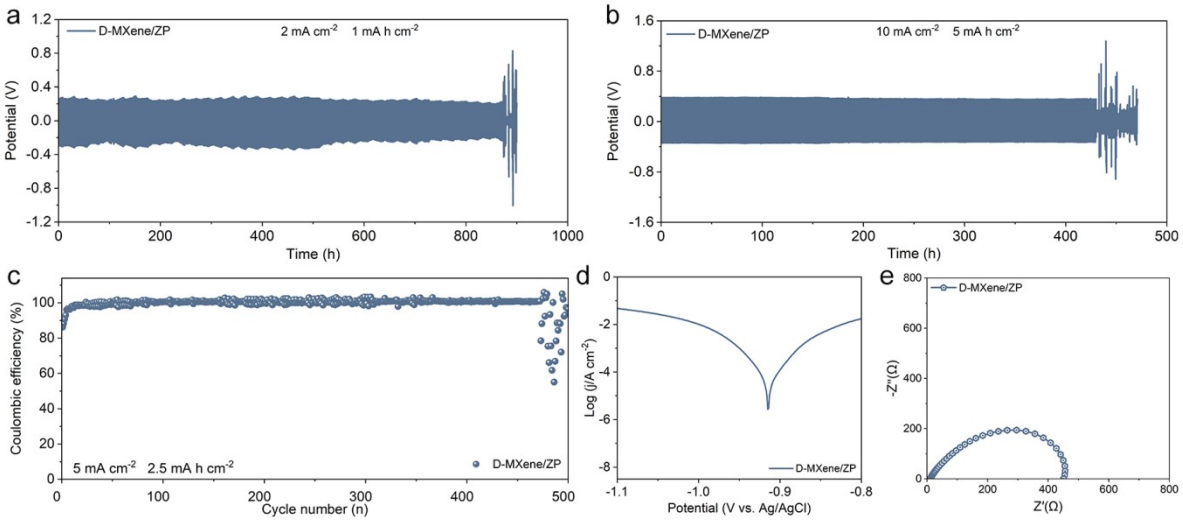

Fig. S17. The electrochemical performance of D-MXene/ZP anode. Long-term cycling voltage profiles of symmetric cells at current density of **a** 2 mA cm^{-2} and **b** 10 mA cm^{-2}.**c** Coulombic efficiencies test. **d** Tafel curves. **e** EIS curves.

As shown in Figure S17a and Figure 3a, the 3D-printed MXene/ZP anode with directional alignment of MXene nanoplates achieves a prolonged cycling lifespan of 1294 h at a current density of 2 mA cm^{-2}, which is markedly superior to the 873 h of the cast D-MXene/ZP counterpart, corresponding to an enhancement of approximately 48.2% in cycling stability. Even at an elevated current density of 10 mA cm^{-2}, the MXene/ZP anode can still sustain stable cycling for 636 h, whereas the D-MXene/ZP anode merely endures 429 h (Figure S17b and Figure 3b). In the Zn||Cu asymmetric cell Coulombic efficiency tests (Figure S17c and Figure 3f), the MXene/ZP anode exhibits excellent electrochemical reversibility, maintaining stable cycling for 832 cycles with a high average CE of 99.62%. In contrast, the cast D-MXene/ZP anode suffers from pronounced CE fluctuations after merely 472 cycles and subsequently fails. This result demonstrates that the directional alignment of MXene nanosheets induced by 3D printing effectively enhances the long-term reversibility of zinc plating/stripping. Figure S17d and Figure S19 present the Tafel polarization curves of the MXene/ZP and D-MXene/ZP anodes. The MXene/ZP anode exhibits a more positive corrosion potential (-0.892 V), which is 23 mV higher than that of the D-MXene/ZP counterpart (-0.915 V). This indicates that the directional alignment of MXene nanosheets can effectively homogenize the interfacial electric field distribution and reduce the exposure of active zinc sites, thereby suppressing zinc self-corrosion and hydrogen evolution reactions. In addition, the EIS curves reveal that the charge transfer resistance of MXene/ZP is 425.2 Ω, while that of D-MXene/ZP is 450.8 Ω (Figure S17e and Figure 3h).

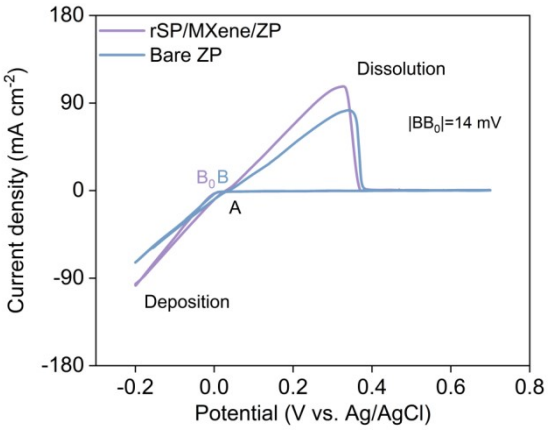

Fig. S18. CV curves of rSP/MXene/ZP and bare ZP anodes.

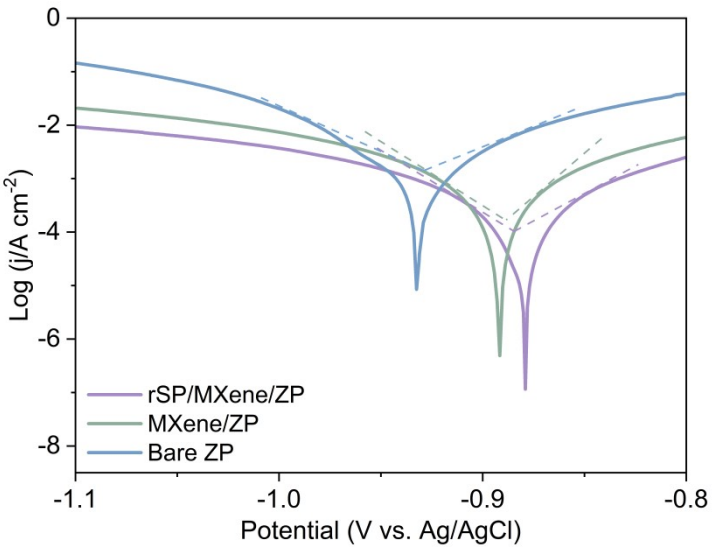

Fig. S19. Tafel curves of rSP/MXene/ZP, MXene/ZP and bare ZP anodes.

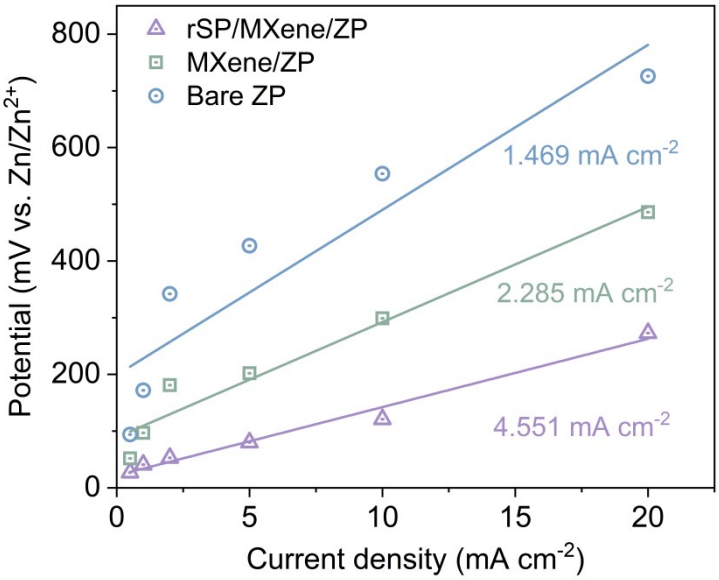

Fig. S20. Exchange current density curves at various rates in rSP/MXene/ZP, MXene/ZP and bare ZP symmetric cells.

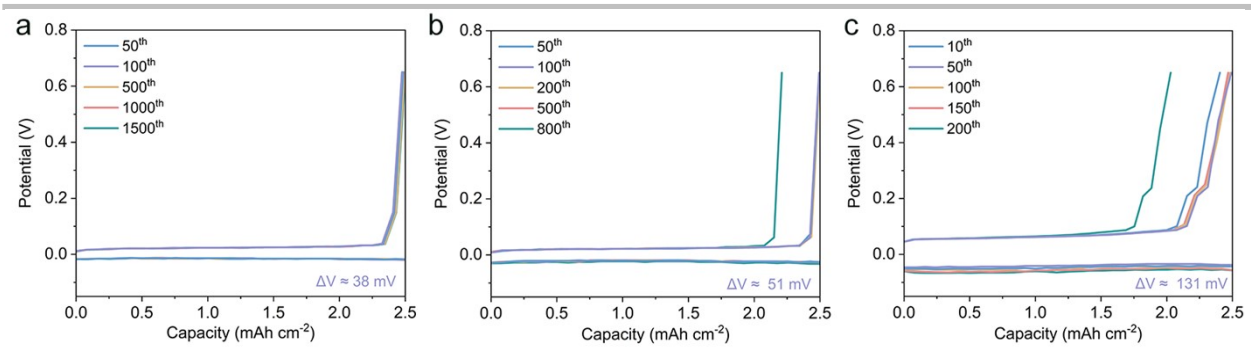

Fig. S21. Voltage profiles of the **a** rSP/MXene/ZP anode and **b** MXene/ZP anode **c** bare ZP anode at 5 mA cm^{-2}.

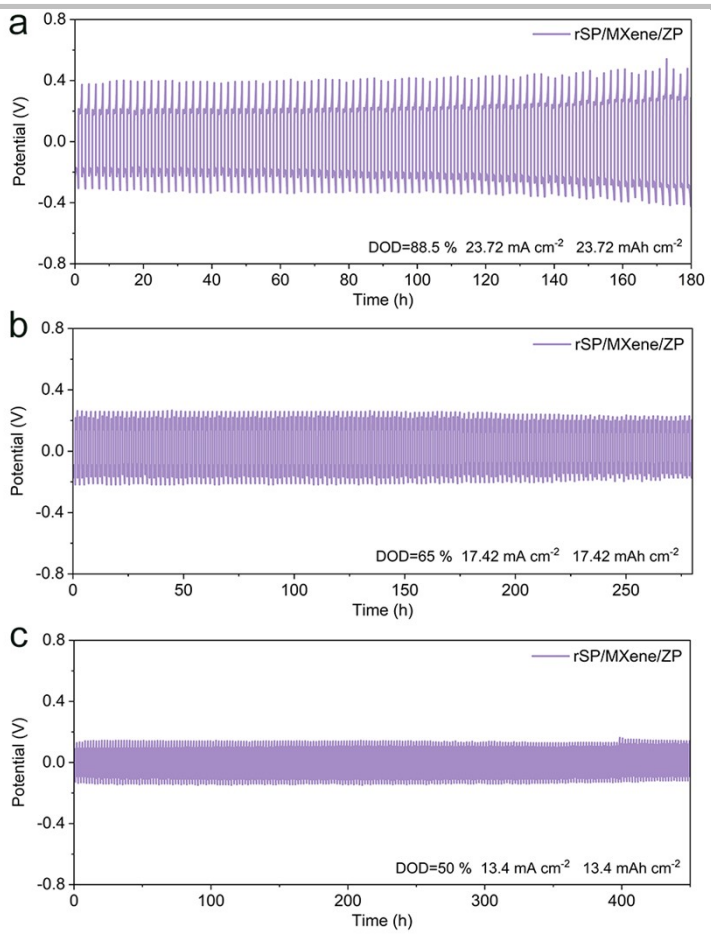

Fig. S22. Long-term galvanostatic cycling of symmetrical rSP/MXene/ZP symmetric cells at high DOD: **a** 88.5%, **b** 65% and **c** 50%.

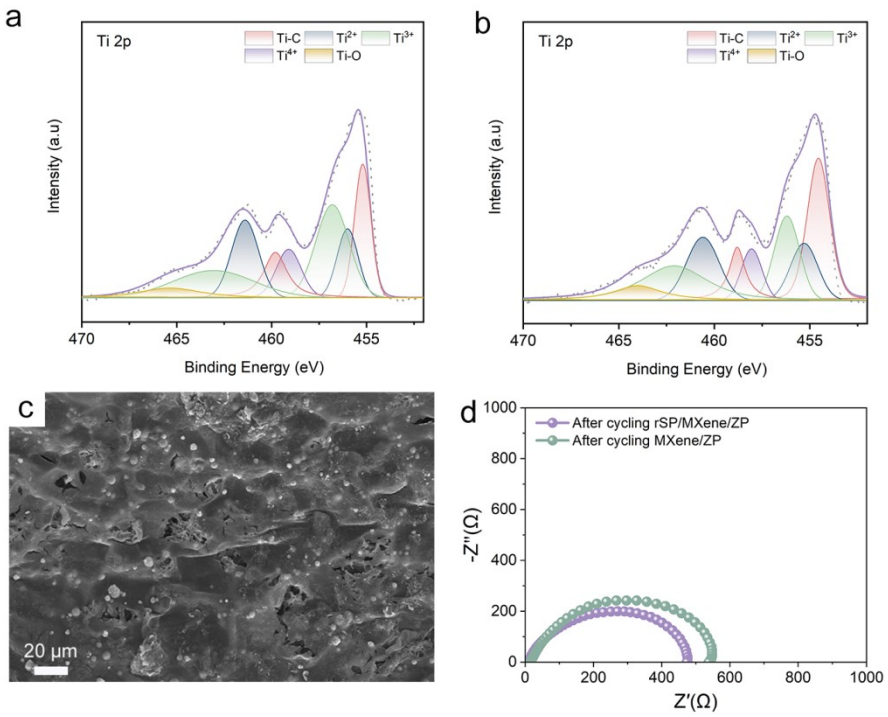

Fig. S23. High-resolution XPS spectrums of rSP/MXene/ZP anode before cycling **a** Ti2p. rSP/MXene/ZP anode after cycling **b** Ti2p. **c** EIS curves of the rSP/MXene/ZP and MXene/ZP anodes after cycling. **d** Cross-sectional SEM image of the rSP/MXene/ZP anode after cycling.

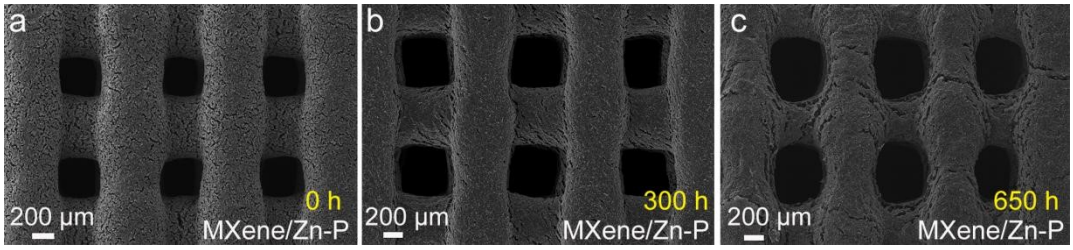

Fig. S24. Ex-situ SEM images of MXene/ZP.

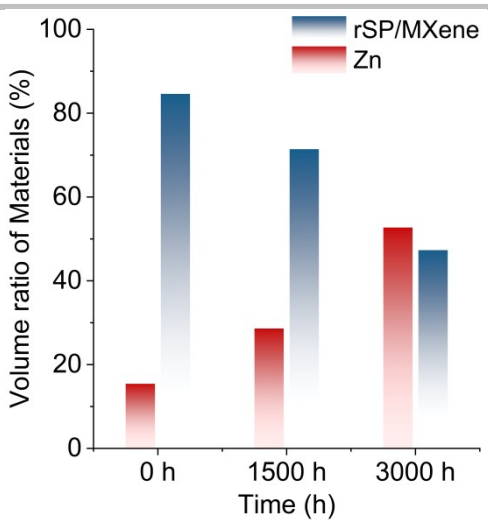

Fig. S25. rSP/MXene/ZP anode at different cycles time corresponding materials volume ratios.

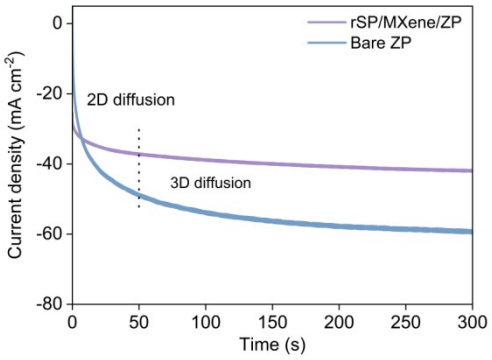

Fig. S26. Chronoamperometry curves of rSP/MXene/ZP and bare ZP anodes.

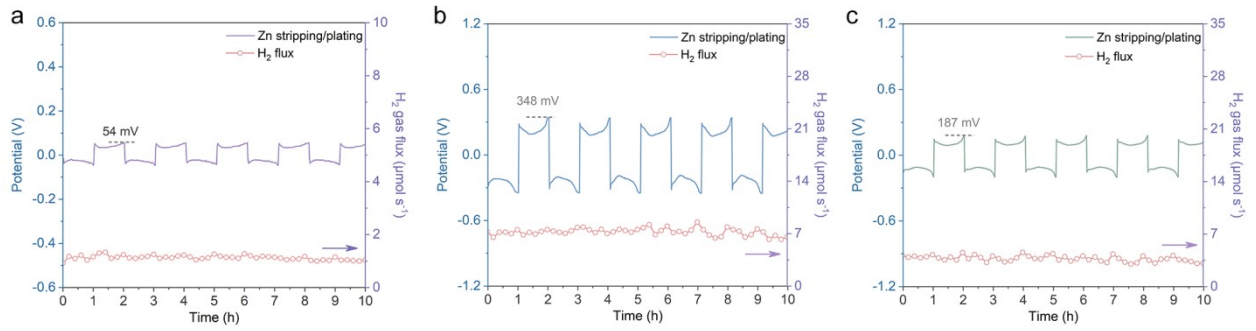

Fig. S27. In-situ monitoring of H_2 evolution flux of **a** rSP/MXene/ZP, **b** bare ZP and **c** MXene/ZP anodes.

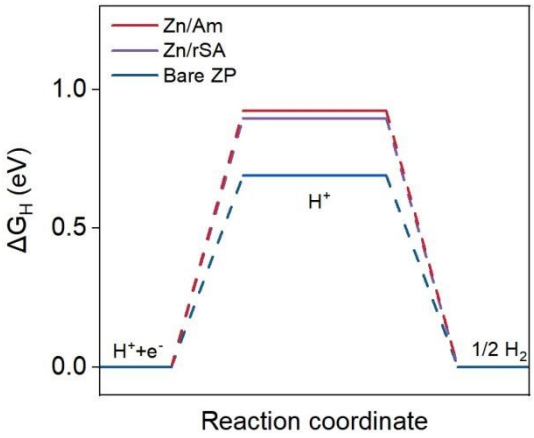

Fig. S28. Calculated H adsorption free energies (ΔG_{H^*}) of bare ZP, Zn/rSA, and Zn/Am.

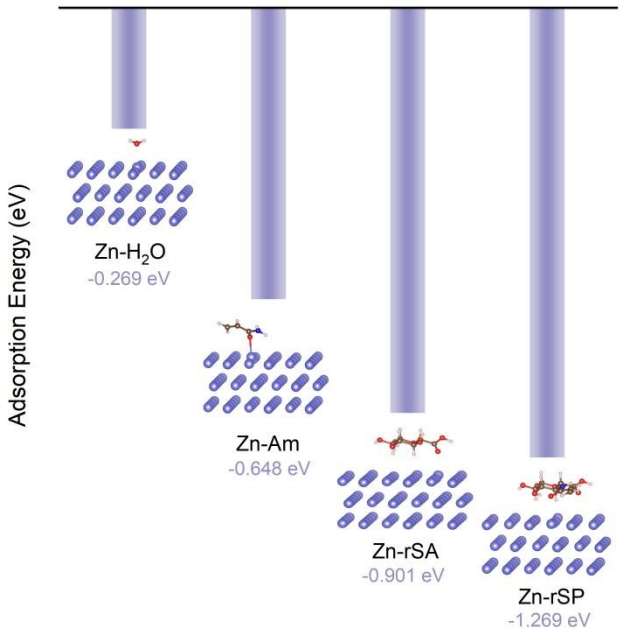

Fig. S29. Adsorption configurations and adsorption energies of H_2O, Am, rSA, and the rSP fragment on Zn(002).

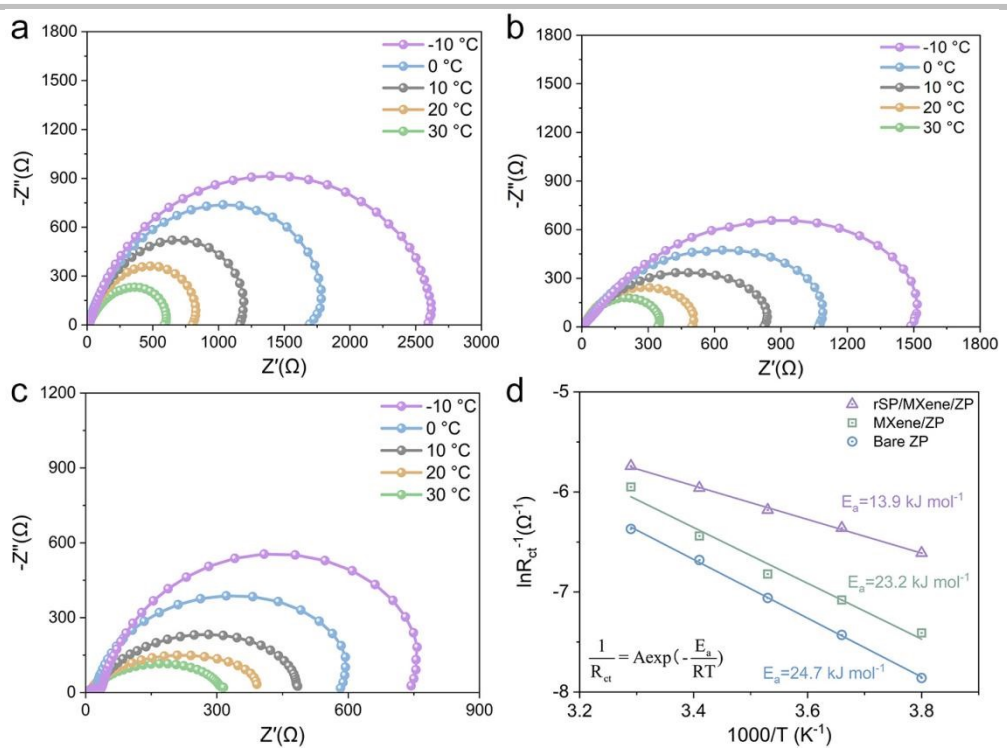

Fig. S30. Nyquist plots at different temperatures for **a** bare ZP, **b** MXene/ZP and **c** rSP/MXene/ZP symmetric cells **d** Corresponding Arrhenius curves and comparison of activation energies.

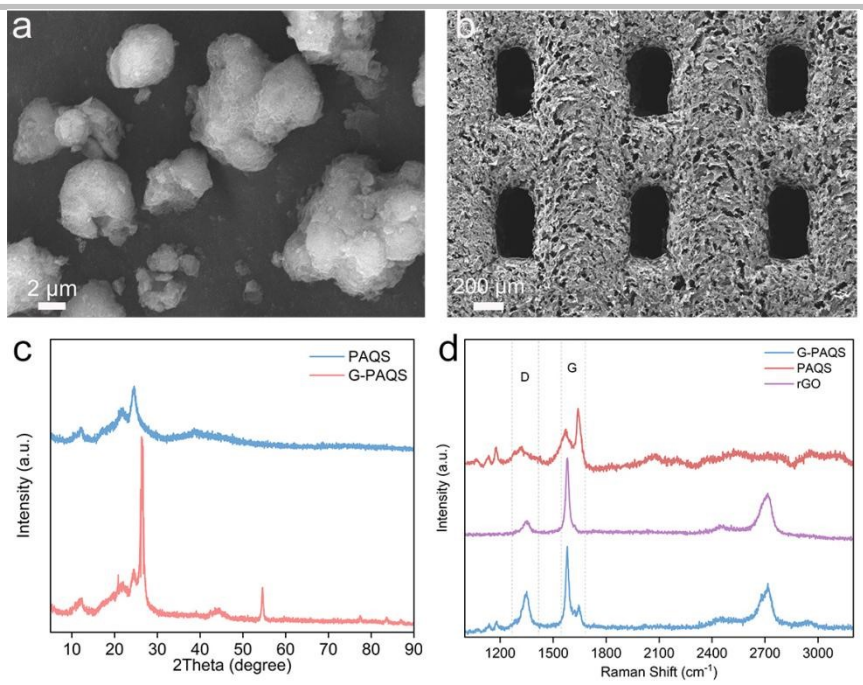

Fig. S31. a SEM images of PAQS and **b** G-PAQS. **c** XRD spectrum of PAQS and G-PAQS. **d** Raman spectrum of G-PAQS, PAQS and rGO.

PAQS can be prepared by polymerizing 2,6-dibromoanthraquinone (2,6-DBrAQ) with sodium sulfide (Na_2S) in anhydrous N-methylpyrrolidone (NMP) solution via a one-pot method. The microstructure of PAQS was characterized by SEM (Fig. S31a). Obviously, the microsphere structure of PAQS is composed of small particles with good uniformity and certain pore structure. Furthermore, PAQS and graphene are prepared into printable ink and PAQS/ graphene (G-PAQS) composite electrode is manufactured by 3D printing technology, which can significantly improve the conductivity of the electrode and realize high-precision and customized electrode manufacturing (Fig. S31b). Besides, the XRD patterns of PAQS and G-PAQS display consistent PAQS characteristic diffraction peaks at 21.7° and 24.3°. For G-PAQS, the characteristic peak of the (002) and (004) plane of graphene appears at 26.3° and 54.9°, respectively (Fig. S31c). The Raman spectrum of PAQS and G-PAQS are shown in Fig. S31d, The characteristic peak at 1316.4 cm^{-1} likely originates from the vibration of C-C bonds in the anthraquinone ring framework. The peak at 1572.5 cm^{-1} represents the symmetric or asymmetric stretching vibrations of C=C bonds in the anthraquinone ring, a typical feature of aromatic conjugated structures. The peak at 1641 cm^{-1} may arise from the stretching vibration of the carbonyl (C=O) group in the anthraquinone ring, which is a characteristic of anthraquinone structures.

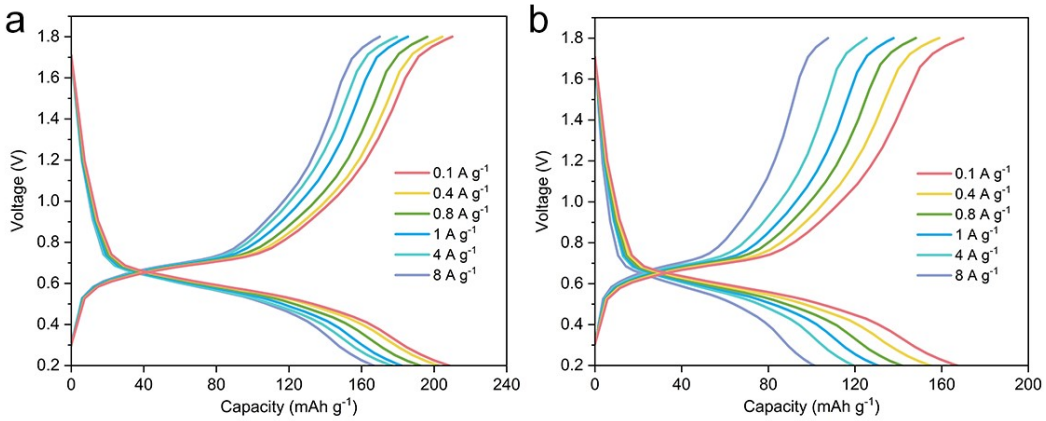

Fig. S32. GCD curves of rSP/MXene/ZP//G-PAQS and bare ZP//G-PAQS full cells.

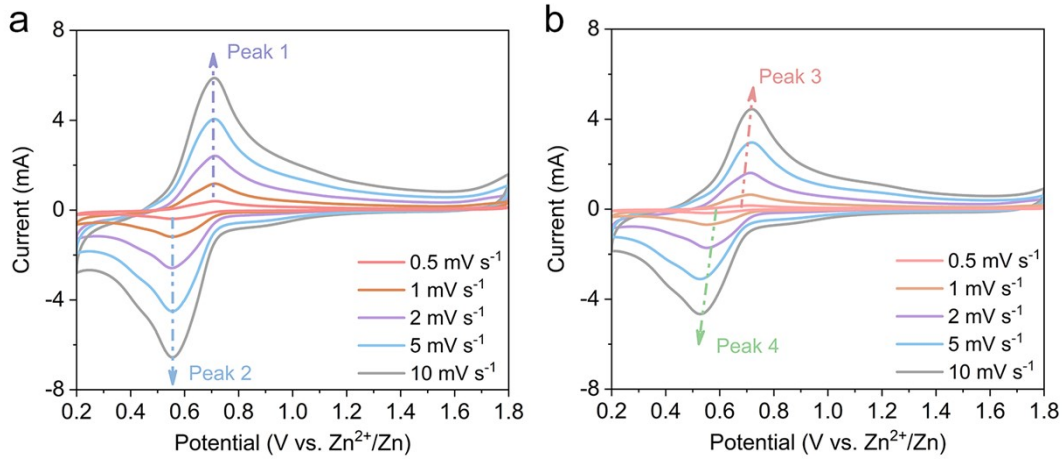

Fig. S33. CV curves of **a** rSP/MXene/ZP//G-PAQS and **b** bare ZP//G-PAQS full cells at different scan rates.

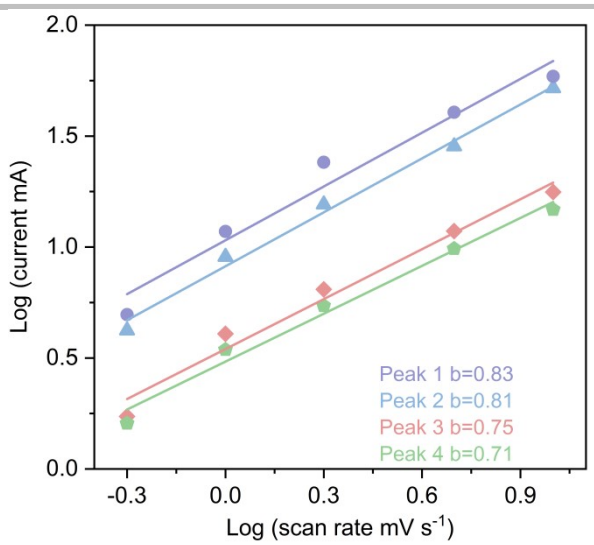

Fig. S34. Log(i) versus log(v) plots at each redox peak.

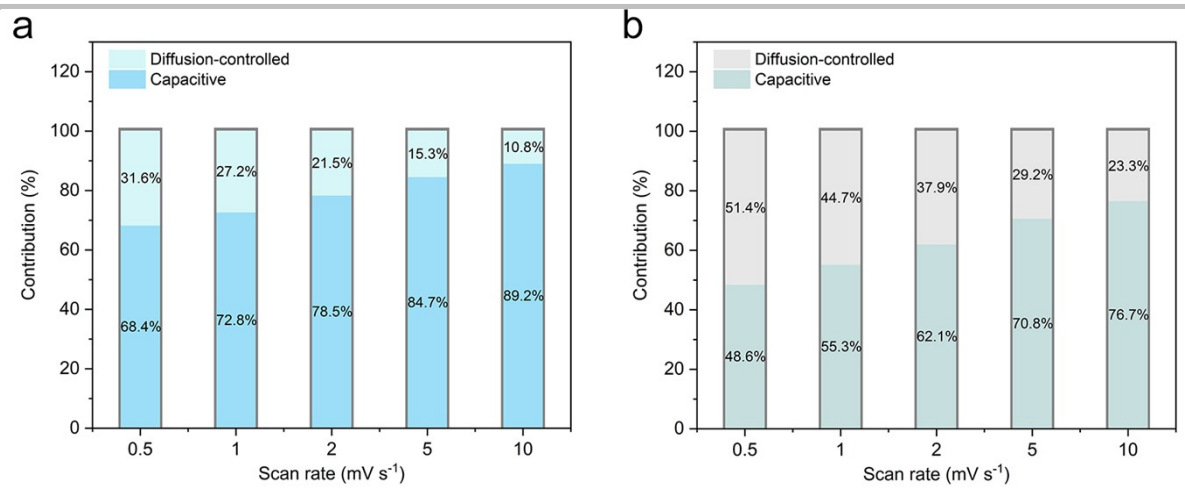

Fig. S35. Normalized capacity contributions of **a** rSP/MXene/ZP//G-PAQS full cell and **b** bare ZP//G-PAQS full cell at different scan rates from 0.5 to 10 mV s^{-1}.

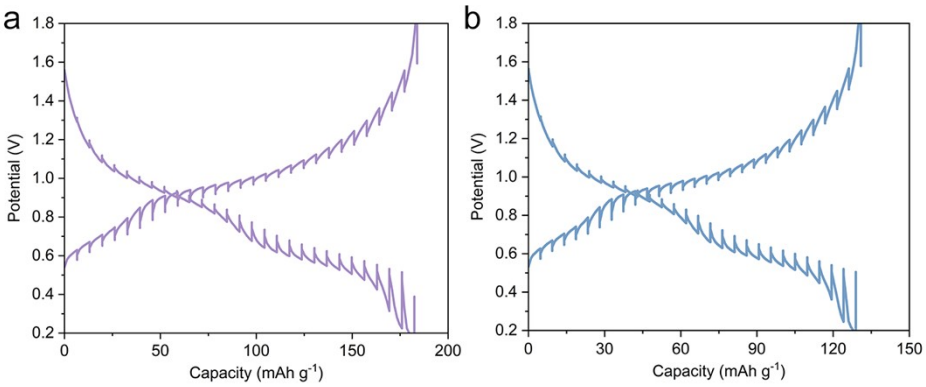

Fig. S36. GITT curves of **a** rSP/MXene/ZP//G-PAQS full cell, **b** bare ZP//G-PAQS full cell at 1 A g^{-1}.

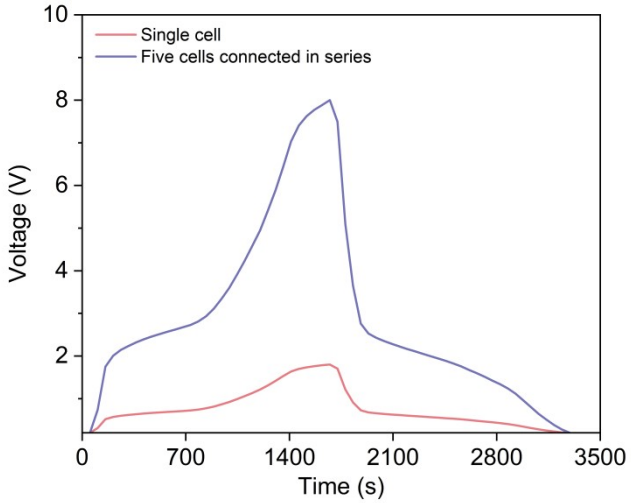

Fig. S37. GCD curves of single cell and five cells connected in series.

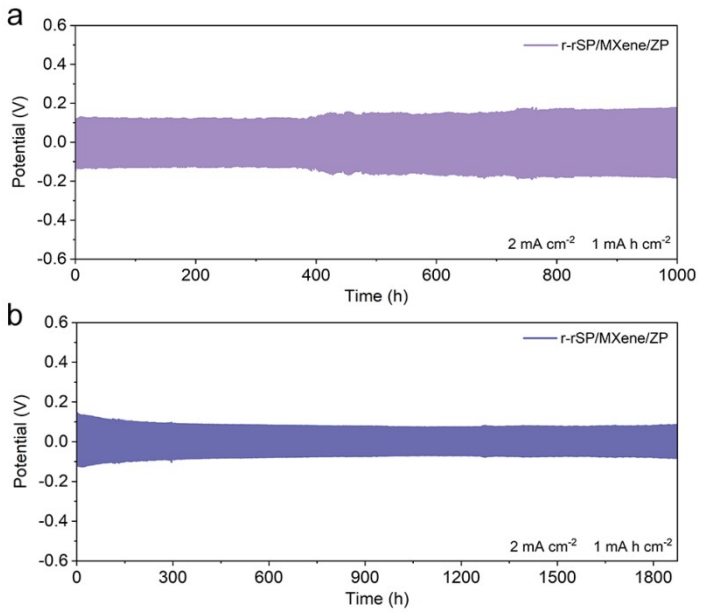

Fig. S38. Voltage profiles of symmetric cells with r-rSP/MXene/ZP anode in **a** $ZnSO_4$ and **b** $Zn(OTf)_2$.

Table S1. Comparison of the DOD and Cumulative capacity of rSP/MXene/ZP Symmetric cell with recently reported Zn||Zn cells.

Anode	Current density (mA cm^{-2})	Areal Capacity (mAh cm^{-2})	Life span (h)	Cumulative plated capacity (mAh)	DOD (%)	Reference
ZnS/Zn/Cu	5	5	300	750	85.5	*Energy Environ. Sci.* ***2024****,17, 1894-1903*
Sn@NHCF	1	1	370	185	8	*Sci. Adv.* ***2022****, 8, eabm5766*
ZF@C-TiO_2	2	2	280	280	10	*Nat. Commun.* ***2020****, 11, 3961*
Zn/CPZ-H	16.4	16.4	225	1845	40	*Nat. Commun.* ***2023****, 14, 4435*
3DCEP-MXene/Zn-P	10	1	250	1250	2.2	*Adv. Mater.* ***2023****, 35, 2209886*
3D Ni-Zn	5	2	200	500	40.6	*Adv. Energy Mater.* ***2021****, 11, 2003927*
Zn/PDZ-H	10	20	280	1400	28	*Adv. Funct. Mater.* ***2022****, 32, 2112540*
TZNC@Zn	4	4	200	400	50	*Angew. Chem. Int. Ed.* ***2022****, 61, e202115649*
1E1M/Zn	1	1	3140	1570	1.8	*J. Am. Chem. Soc.* ***2024****, 146, 30998-31011*
Zn@PFSA	1	1	800	400	5.6	*ACS Nano* ***2022****, 16, 6906-6915*
SDF/Zn	3	4.5	250	375	45	*Adv. Energy Mater.* ***2021****, 11, 2100214*
CuNBs@NCFs-Zn	5	2	250	625	25	*Adv. Mater.* ***2022****, 34, 2200342*
Sn@Zn-IP	2	1	700	700	0.9	*Adv. Funct. Mater.* ***2022****, 32, 2205771*
BPE/Zn	0.2	0.2	6000	600	2	*Adv. Mater.* ***2024****, 36, 2304426*

$Zn@ZnF_2$	0.5	1	500	125	1.7	*Adv. Mater.* ***2021****, 33, 2007388*
$Zn(TFSI)_2$-sulfolane-H_2O/Zn	0.5	0.5	4400	1730	0.85	*Angew. Chem. Int., Ed.* ***2023****, 62, e202215552*
ILG/Zn	0.1	0.1	1000	50	12.1	*Adv. Funct. Mater.* ***2021****, 31, 2103850*
Zn-P-MIEC	0.25	0.05	1250	50	5.6	*Adv. Mater.* ***2022****, 34, 2200860*
PT-ZHC-Sn@Zn	0.5	0.5	6500	1625	4.3	*Adv. Mater.* ***2024****, 36, 2406093*
rSP/MXene/ZP	23.72	23.72	180	2135	88.5	Our work

Table S2. Lifespan comparison between this work and recently published studies.

Anode	Current density (mA cm^{-2})	Areal Capacity (mAh cm^{-2})	Life span (h)	Reference
ZnS/Zn/Cu	5	5	300	*Energy Environ. Sci.* ***2024****,17, 1894-1903*
Sn@NHCF	1	1	370	*Sci. Adv.* ***2022****, 8, eabm5766*
HCS/Zn	1	0.5	2700	*Mater. Today Energy* ***2024****, 46, 101736*
M3DP-MXene/Cu-THBQ/Zn-P	2	1	1800	*Adv. Mater.* ***2024****, 36, 2309753*
3DCEP-MXene/Zn-P	1	0.5	655	*Adv. Mater.* ***2023****, 35, 2209886*
3D Ni-Zn	5	2	200	*Adv. Energy Mater.* ***2021****, 11, 2003927*
Zn/PDZ-H	2	4	1350	*Adv. Funct. Mater.* ***2022****, 32, 2112540*
Zn@PFSA	1	1	800	*ACS Nano* ***2022****, 16, 6906-6915*
Sn@Zn-IP	2	1	700	*Adv. Funct. Mater.* ***2022****, 32, 2205771*
Zn@ZnF_2	0.5	1	500	*Adv. Mater.* ***2021****, 33, 2007388*
Bilayer SEI/Zn	2	1	1600	*Nat. Commun.* ***2024****, 15, 8431*
MPVMT@Zn	1	1	2000	*Nat. Commun.* ***2024****, 15, 753*
ZAP@Zn@Cu	1	1	2100	*Adv. Mater.* ***2024****, 36, 2312934*
CNT guard-Zn	2	1	1850	*Adv. Energy Mater.* ***2023****, 13, 2203165*

KI-CHOP@Zn	1	1	2250	*Energy Storage Mater.* ***2024****, 72, 103769*
rSP/MXene/ZP	23.72	23.72	3000	Our work

Table S3. Comparison of the assembled rSP/MXene/ZP//G-PAQS full cell with the previously reported aqueous Zn ion battery.

Cathode	Anode	Electrolyte	Current Density	Capacity	Life	Energy/Power Density	Reference
3DCEP-MXene/Co-MnHCF	3DCEP-MXene/ Zn-P	PAAm-3M $Zn(OTf)_2$	0.2 A g^{-1}	218.4 mAh g^{-1}	95.7% after 1600 cycles at 2 A g^{-1}	283.92 Wh Kg^{-1} 141.96 W Kg^{-1}	*Adv. Mater.**2022**, 2209886*
MnO_2@C/PVDF-Sn	Zn Foil	2M $ZnSO_4$	2 A g^{-1}	195.6 mAh g^{-1}	70.3% after 700 cycles at 2 A g^{-1}	211.4 Wh Kg^{-1} 377.5 W Kg^{-1}	*Nat. Commun. **2023**,14:641*
NVO	Zn/HE	DMAC/TMP /H_2O and 1M $Zn(OTf)_2$	0.5 A g^{-1}	170.9 mAh g^{-1}	71.4% after 3000 cycles at 0.5 A g^{-1}	77 Wh Kg^{-1} 665 W Kg^{-1}	*Nat. Commun. **2023**,14:2720*
I_2	Zn//B	2 M $ZnSO_4$ + 10 mM DMI + 0.5 M $ZnBr_2$	2.1 A g^{-1}	151.2 mAh g^{-1}	90% after 5000 cycles at 2.1 A g^{-1}	241.6 Wh Kg^{-1} 990.3 W Kg^{-1}	*Nat. Commun. **2024**,15:8431*
NVO	ZnS/Zn/ Cu	2M $ZnSO_4$	2 A g^{-1}	193.5 mAh g^{-1}	77.6% after 1400 cycles at 2 A g^{-1}	177.1 Wh Kg^{-1} 506 W Kg^{-1}	*Energy Environ. Sci. **2024**, 17, 1894-1903*
PANI/CC	3DP-ZA	3M $Zn(OTf)_2$	1 A g^{-1}	167.1 mAh g^{-1}	81.6% after 1000 cycles at 1 A g^{-1}	183.7 Wh Kg^{-1} 522.5 W Kg^{-1}	*Energy Storage Mater. **2023**, 54 469-477*
G/TEMPO	M3DP-MXene/ Cu-THBQ/Zn-P	3M $Zn(OTf)_2$	4 A g^{-1}	235.4 mAh g^{-1}	96.8% after 1200 cycles at 4 A g^{-1}	329.8 Wh Kg^{-1} 218.4 W Kg^{-1}	*Adv. Mater. **2024**, 36, 2309753*
$K_2MnFe(CN)_6$	Zn Foil	30 M KFSI+1 M $Zn(CF_3SO_3)_2$	0.2 A g^{-1}	138 mA h g^{-1}	83% after 400 cycles at 0.2 A g^{-1}	150 Wh Kg^{-1} 187.5 W Kg^{-1}	*Adv. Energy Mater.* **2021**, 2003639

MnO_2	SDF	2 M $ZnSO_4$ and 0.1 M $MnSO_4$	0.3 A g^{-1}	213 mAh g^{-1}	97.6 % after 800 cycles at 3 A g^{-1}	212.81 Wh Kg^{-1} 103.8 W Kg^{-1}	*Adv. Energy Mater.* **2021**, *11, 2100214*
$Cu_3(HHTP)_2$	Zn foil	3M $Zn(CF_3SO_3)_2$	0.1 A g^{-1}	189.2 mAh g^{-1}	75 % after 500 cycles at 4 A g^{-1}	151.4 Wh Kg^{-1} 75.61 W Kg^{-1}	*Nat. Commun.* **2019** *10:4948*
$Zn_3V_3O_8$	Zn foil	21 M $LiN(CF_3SO_2)_2$ +1 M $Zn(CF_3SO_3)_2$	0.15 A g^{-1}	127 mAh g^{-1}	72.6 % after 2000 cycles at 5 A g^{-1}	190.5 Wh Kg^{-1} 86.59 W Kg^{-1}	*Energy Storage Materials* **2021** *41 297–309*
$CoFe(CN)_6$	Zn Foil	4 M $Zn(OTf)_2$	0.3 A g^{-1}	173.4 mAh g^{-1}	2200 cycles at 3 A g^{-1}	260.1 Wh Kg^{-1} 104.04 W Kg^{-1}	*Adv. Energy Mater.* **2019**, *1902446*
LMO	PCu@Zn	2 M $ZnSO_4$	0.45 A g^{-1}	84 mAh g^{-1}	77.6 % after 300 cycles at 0.148 A g^{-1}	50.82 Wh Kg^{-1} 23.15 W Kg^{-1}	*Adv. Mater.* **2022**, *34, 2200782*
NVPOF	Zn Foil	0.5 M Zn^{2+} and 1.0 M Na^+ in TMP	0.2 C	113 mAh g^{-1}	83.5 % after 1000 cycles at 1.0 C	203 Wh Kg^{-1} 145 W Kg^{-1}	*J. Mater. Chem. A,* **2020**, *8, 3252–3261*
V_2O_5	3DP-PC/SiOC @Zn	3 M $ZnSO_4$	129.3 mA g^{-1}	0.5 A g^{-1}	76.5 % after 500 cycles at 0.45 A g^{-1}	232.8 Wh Kg^{-1} 155.2 W Kg^{-1}	*Nano Energy* **2020**, *100, 107505*
G-PAQS	rSP/MXene/ZP	3 M $Zn(OTf)_2$	0.1 A g^{-1}	208.2 mAh g^{-1}	89.4% after 10560 cycles at 4 A g^{-1}	333.1 Wh Kg^{-1} 406.2 W Kg^{-1} And 266.9 Wh Kg^{-1} 1270.9 W Kg^{-1}	Our work

References:

[1] G. Kresse, J. Furthmuller, *Phys. Rev. B* **1996**, *54*, 11169.

[2] M. J. Frisch, G. W. Trucks, H. B. Schlegel, **2009**.

[3] K. B. M. E. John P. Perdew, *Phys. Rev. Lett.*, *77*, 3865.

[4] D. Vanderbilt, *Phys. Rev. B* **1990**, *41*.

[5] S. Grimme, J. Antony, S. Ehrlich, H. Krieg, *J. Chem. Phys.* **2010**, *132*, 154104.

[6] A. D. Becke, *The Journal of Chemical Physics* **1992**, *96*, 2155.